



Vanadyl ethylene glycolate: A novel organic-inorganic electrode material for rechargeable aqueous aluminum-ion battery

Sunny Nandi^{a,c}, Yichen Yan^b, Xintong Yuan^c, Chongzhen Wang^c, Ximin He^b, Yuzhang Li^{c,*}, Shyamal K. Das^{a,*}

^a Department of Physics, Tezpur University, Assam 784028, India

^b Department of Materials Science and Engineering, University of California, Los Angeles 90095, United States

^c Department of Chemical and Biomolecular Engineering, University of California, Los Angeles 90095, United States

ARTICLE INFO

Keywords:

Aluminum-ion battery
Vanadyl ethylene glycolate
Aqueous electrolyte

ABSTRACT

This report illustrates an investigation on the electrochemistry of vanadyl ethylene glycolate (VEG) for rechargeable aqueous aluminum-ion battery for the first time. Vanadyl ethylene glycolate nanorods were synthesized by in-situ deposition on a carbon cloth current collector and, thereby, it makes a binder free electrode. It is found that the binder free VEG could significantly improve the electrochemical stability in comparison to pristine VEG with binder due to intimate contact of the electrode material with the current collector which resulted in reduced charge transfer resistance. The binder free electrode could deliver a stable discharge capacity of 77 mAhg⁻¹ over 600 cycles at a high current density of 2 Ag⁻¹, whereas pristine VEG shows negligible specific capacity. The Al³⁺ ion storage mechanism is also demonstrated utilizing ex-situ XPS, XRD and electron microscopy techniques.

1. Introduction

Multivalent ion batteries are offering exciting opportunities in the field of electrochemical energy storage [1–4]. The enthusiasm is primarily driven by the relative high abundance and low-cost of multivalent ion resources alongside the ability to offer more than one redox electron per multivalent cation. Zn²⁺ ion and Mg²⁺ ion batteries are the two most investigated multivalent systems. Besides having challenges for the formulations of a compatible electrolyte for these systems, appropriate selection of an efficient electrode material is also an arduous task [3–6]. In this context, vanadium-based materials have been studied extensively [6–9]. The multiple oxidation states of vanadium (+2 to +5) can support redox reactions with multi electron transfer. Vanadium oxides, vanadium phosphates and metal/nonmetal vanadates have shown to electrochemically store Zn²⁺ and Mg²⁺ ions [9].

Similarly, battery chemistries based on trivalent Al³⁺ ion have also gained significant interest [10–25]. In this case, V₂O₅ was the initial cathode material where reversible Al³⁺ ion insertion in nonaqueous chloroaluminate ionic liquid electrolyte was demonstrated [18]. Thereafter, there have been attempts to show Al³⁺ ion insertion/extraction in aqueous electrolytes for a few electrode materials

including V₂O₅ [18–24]. On the other hand, there is a class of hybrid material composed of inorganic and organic components known as vanadyl ethylene glycolate (VO(CH₂O)₂), abbreviated as VEG, where Al³⁺ ion storage behavior has not yet been investigated. The crystal structure resembles a one-dimensional chain which consists of VO₅ square pyramid and chelating ligand (-OCH₂CH₂O-). The detailed structural analysis was performed by the group of Whittingham [26]. There are sporadic reports for the investigation of Li⁺ and Zn²⁺ ion storage in VEG [27–30]. For example, Wang et al. showed that the Li⁺ ion kinetics in VEG could be enhanced significantly by the presence of the organic ligand [27]. It was also demonstrated that VEG maintains specific capacity of 550 mAhg⁻¹ at current rate of 1 Ag⁻¹ for over 2000 cycles. Li et al. demonstrated the performance of lithium-ion battery with VEG. It was shown that VEG could deliver high specific capacities and a capacity of 477 mAh g⁻¹ could be achieved over 200 cycles at a current rate of 60 mAhg⁻¹ [28]. Similarly, Nagaraj et al. demonstrated the performance of an aqueous zinc-ion battery with VEG as a cathode material. A discharge capacity of above 100 mAhg⁻¹ was obtained over 2000 cycles at a current rate of 4 Ag⁻¹ [29]. Furthermore, Li et al. also reported a high storage capacity and good cycling stability for Zn²⁺ ion storage at high current rates [30]. These studies encourage us to

* Corresponding authors.

E-mail addresses: yuzhangli@ucla.edu (Y. Li), skdas@tezu.ernet.in (S.K. Das).

investigate the electrochemical behavior of VEG for aqueous aluminum-ion battery chemistries.

Herein, we report the electrochemical investigation of VEG in Al^{3+} ion conducting aqueous electrolyte for the first time. We also show that in-situ grown VEG on carbon cloth substrate exhibits better electrochemical performance than the pristine form of VEG.

2. Experimental

Vanadyl ethylene glycolate was prepared using a one-step hydrothermal method as reported in ref. [29]. Briefly, to describe, 0.58 g of NH_4VO_3 was added in 30 ml of ethylene glycol and stirred vigorously for 1 h. Then, the obtained solution was transferred to a Teflon-lined stainless-steel autoclave and maintained at 120 °C for 24 h and then cooled down naturally to room temperature. The resulting product was separated, washed with distilled water and ethanol several times, and dried at 90 °C for 12 h. Electrode slurry was prepared by mixing VO $(\text{CH}_2\text{O})_2$ powder, carbon black and polyvinylidene fluoride in a weight ratio of 7:2:1 using *N*-methyl-2-pyrrolidone solvent. The slurry was drop cast on pristine carbon cloth (purchased from Fuel cell store, USA, ELAT hydrophilic, Product code: 1591002, 14 mm in diameter) abbreviated as VEG/CC and dried at 90 °C for 12 h. For the preparation of binder free vanadyl ethylene glycolate electrode, few pieces of carbon cloth (14 mm in diameter) were dipped in the above mixture solution and performed the hydrothermal treatment as described above. The binder free electrode was collected after the treatment, washed with distilled water/ethanol for few times and finally dried at 90 °C for 12 h and abbreviated as bf-VEG/CC in the manuscript. It is to be noted here that there is no control of mass loading on the binder free electrodes. Therefore, for the estimation of the accurate mass loading, the bare carbon substrates were marked before doing the in-situ synthesis for identification. The weights of these bare substrates were noted down before placing them inside the autoclave. After the synthesis, the weights of these electrodes were again noted. Based on the identification marks, the actual weight was estimated by noting the difference between the weights. The weight of the active material varies from 2.5 mg to 3.5 mg.

For the electrochemical analysis, cyclic voltammetry (CV) and galvanostatic discharge/charge experiments were conducted in a conventional three-electrode electrochemical glass cell where Pt electrode and Ag/AgCl electrode were used as the counter and reference electrodes, respectively. The used electrolyte was 1 M AlCl_3 unless otherwise specially stated. The amount of electrolyte used in all the experiments was 5 ml. For consistency of the acquired data, the electrodes (i.e. working, reference and counter) were placed in a triangular configuration with a separation of 1 cm between all of them. All the electrodes were dipped in the electrolyte up to 1 cm of depth. The discharge/charge and CV experiments were performed in a voltage range of -0.3 to 1 V (vs. Ag/AgCl). Electrochemical impedance spectra (EIS) were recorded in frequency range of 1 mHz–200 kHz at 10 mV signal amplitude. All the electrochemical tests were performed at room temperature (25 °C).

The material was analyzed using powder X-ray diffraction (Rigaku Miniflex II diffractometer with $\text{Cu K}\alpha$ radiation operated at 30 kV and 15 mA, Raman spectra were recorded on a Renishaw 2000 system using a laser wavelength of 633 nm. The morphologies of the samples were characterized using field emission electron microscopy (ZEISS Supra 40 V) and transmission electron microscopy (TEM, JEOL-2010 F). X-ray photoelectron spectroscopy (XPS) analysis was performed by the AXIS Ultra DLD system. Thermogravimetric analysis (TGA) was performed under an air flow (50 ml min^{-1}) and ramping rate of $10 \text{ }^\circ\text{C min}^{-1}$ with Netzsch STA 449 F3 Jupiter.

3. Results and discussion

VEG nanorod was synthesized using a one-step glycothermal method following a protocol as reported in ref. [29]. Binder free VEG electrodes were also glycothermally prepared by growing in-situ VEG nanorods on

plasma treated carbon cloth substrate. The carbon cloth was treated with oxygen plasma for 20 min in order to improve hydrophilicity and electrolyte wettability on the surface of the carbon cloth. Fig. 1a shows the XRD patterns of the VEG nanorods and bf-VEG/CC. It could be seen that the diffraction peaks are mostly matching with the monoclinic crystal phase of VEG with a space group C2/c (JCPDS no. 49–2497) for both the synthesized products. Fig. 1b shows the Field emission scanning electron microscope (FESEM) image of the synthesized VEG and it clearly indicates formation of nanorods. Fig. 1 (c-d) shows the FESEM image of pristine carbon cloth. Fig. 1 (e-f) shows the FESEM images of binder free VEG nanorods on carbon cloth. FESEM image of VEG nanorods coated on carbon cloth using PVDF as binder (abbreviated as VEG/CC) is also shown in Fig. S1. The carbon cloth is composed of micron size carbon fibers of high aspect ratio. As could be observed in Fig. 1 (e-f), VEG nanorods are firmly organized around the carbon fiber in the case of bf-VEG/CC. On the other hand, VEG nanorods are randomly distributed over the carbon fibers and wrapped in PVDF layer in the case of VEG/CC (Fig. S1). TEM image of VEG nanorod is shown in Fig. S2. Thermogravimetric analysis (TGA) clearly shows the decomposition of the organic component present in VEG at temperature of 225 °C (Fig. S3).

Fig. 2a shows the CV profiles of bf-VEG in 1 M AlCl_3 aqueous electrolyte at a scan rate of 2.5 mVs^{-1} in a voltage range of -0.3 V to 1 V (vs. Ag/AgCl). Clearly, redox activities are prominently noticeable. A pair of cathodic (peak A) and anodic (peak B) redox peaks are observed around 0.25 V and 0.50 V respectively. It appears that peak A may be a superimposition of two redox peaks. Similar redox activities are also observed in case of VEG/CC except peak A' seems to be composed of only one peak (Fig. 2b). It is noted that the CV profiles in both the cases are highly reversible for the measured number of scans and it may be ascribed to continuous and facile insertion/deinsertion of Al^{3+} ion in the VEG structure. This behavior is in contrast to the Zn^{2+} ion intercalation/deintercalation phenomenon in VEG where two pairs of prominent cathodic and anodic redox peaks are always observed [29–30].

Fig. 2 (c, d) shows the galvanostatic charge/discharge profiles of bf-VEG and VEG in 1 M AlCl_3 aqueous electrolyte at a specific current rate of 2 Ag^{-1} . As could be seen, there is no perfectly flat discharge/charge potential plateaus. Rather a short discharge plateau around 0.2 V could be noticed in both cases. Similarly, a small charge plateau around 0.34 V could be seen. The galvanostatic profiles are in consistent with the respective CV profiles. The initial discharge and charge capacities of bf-VEG were 346 mAhg^{-1} and 277 mAhg^{-1} , which are much higher than the capacities obtained from VEG/CC (Fig. 2d). The VEG/CC electrode delivered an initial discharge and charge capacities of only 35 mAhg^{-1} and 24 mAhg^{-1} at the identical current rate. The variation of discharge capacity with cycle number is shown in Fig. 2e. It is obvious that the binder free electrode shows better cycling stability than VEG/CC. It is observed that binder free electrode could maintain a discharge capacity of 77 mAhg^{-1} over 600 cycles at a specific current rate of 2 Ag^{-1} and even at high current rate of 2.5 Ag^{-1} (Fig. S4), it could still deliver a discharge capacity around 41 mAhg^{-1} over 500 cycles. On the contrary, pristine form of VEG shows negligible specific capacities ($\sim 2.3 \text{ mAhg}^{-1}$). This significant improvement in electrochemical performance may be attributed to the intimate electrochemical contact between the electrode and current collector, which is also supported by the EIS data. The EIS data are fitted with an equivalent circuit and it is shown in Fig. 2f and Fig. S5. It is found that the binder free electrode displays much lower charge transfer resistance ($3.39 \text{ k}\Omega \text{ cm}^{-2}$) than pristine VEG ($32.95 \text{ k}\Omega \text{ cm}^{-2}$). In order to get an assurance of correct estimation of specific capacities, CV and galvanostatic charge-discharge experiments were performed with the pristine form of carbon cloth in 1 M AlCl_3 aqueous electrolyte at identical current rate shown in Fig. S6. These measurements rule out the possible electrochemical activity of the carbon cloth current collector. Therefore, it is certain that the electrochemical behavior is only due to VEG.

For a comparison, CV experiments were also performed with binder free VEG electrode in 1 M LiCl, 1 M NaCl and 1 M MgCl_2 aqueous

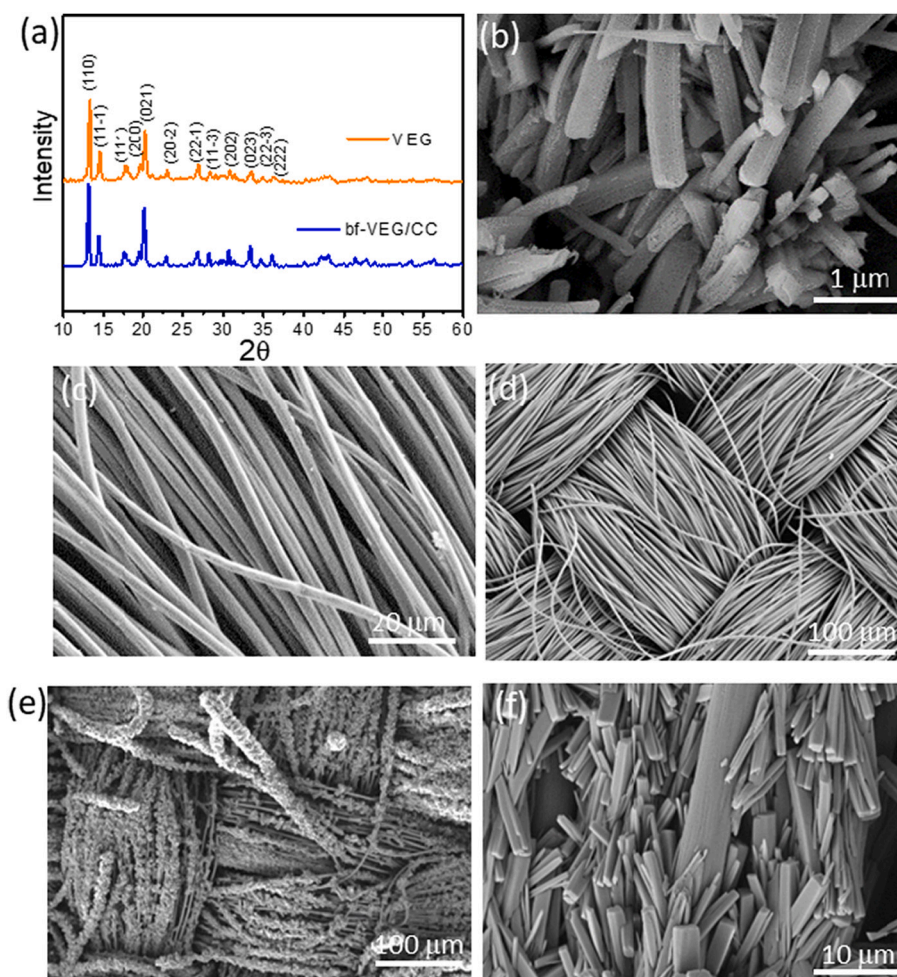


Fig. 1. (a) XRD patterns, and SEM images of (b) VEG nanorods, (c-d) pristine carbon cloth, and (e, f) bf-VEG/CC.

electrolytes at a scan rate of 2.5 mVs^{-1} which are shown in Fig. 3. It is evident from the CV profiles that bf-VEG/CC shows a completely different behavior in Al^{3+} ion aqueous electrolyte than the rest of the investigated ions. There is no signature of prominent redox activities in these electrolytes unlike the case of Al^{3+} ion. Similar behavior was also observed for MoO_3 and WO_3 [31–34]. A straightforward analysis is difficult here. The ionic radii of Li^+ , Na^+ , Mg^{2+} and Al^{3+} are 0.6 \AA , 0.95 \AA , 0.65 \AA and 0.5 \AA respectively [35]. It is tempting to infer that the Al^{3+} ion insertion process is easier since the ionic radius is smaller in case of Al^{3+} ion. However, since aqueous medium is used in the electrolyte, the metal ions are solvated by water molecules and, therefore, the effect of hydrated ions should not be ruled out. The hydrated radii of Li^+ , Na^+ , Mg^{2+} and Al^{3+} are 3.82 \AA , 3.58 \AA , 4.28 \AA and 4.75 \AA respectively [35]. Al^{3+} ion has the largest hydrated radius. It is unknown to us at this juncture how the hydrated ion communicates at the electrode-electrolyte interface. A detailed computational analysis is required to determine the hydration energies, the hydrodynamic behavior and the charge transfer process at the electrode-electrolyte interface in order to accurately understand this complex electrochemical process.

In order to examine any possible structural and morphological changes of VEG during the electrochemical processes, post-mortem analysis of the electrodes was performed by spectroscopic and electron microscopic techniques. As shown in Fig. 4a, the ex-situ XRD patterns indicate that there are no characteristic diffraction peaks of VEG in harvested VEG electrode after 1st discharge and 1st charge. The broad peak which appeared at $2\theta = 26.15^\circ$ is basically the characteristic diffraction peak of the carbon cloth. Ex-situ FESEM images (Fig. 4b and Fig. S7) also show a complete morphological change of the electrode

after discharge. The one-dimensional VEG structure transformed to a polymeric layer type material after charge/discharge. Similarly, the ex-situ TEM analysis also indicates the complete loss of nanorod morphology and amorphous aggregated clusters could be noticed (Fig. 4c). All these measurements signify the transformation of the crystalline VEG into an amorphous phase after the Al^{3+} ion electrochemical processes. Ex-situ XPS was also conducted to probe the valence states of V 2p during the electrochemical processes. As shown in Fig. 5a, the pristine VEG electrode exhibits two major peaks at 517.2 eV and 524.3 eV that are assigned to V 2p_{3/2} and V 2p_{1/2} components of V^{4+} [36]. However, after the 1st discharge state, the V2p shifted to lower energy suggesting the reduction of V^{4+} to V^{3+} . Similar behavior is observed after the 1st charge. This indicates that a mixed valence state exists in the electrochemical processes. Moreover, the appearance of Al 2p peak at 74.6 eV indicates presence of Al in the discharged electrode (Fig. 5b). The presence of Al^{3+} ions in the discharged/charged state VEG electrode is also supported by the quantitative elemental mapping (Fig. S8). The mapping shows presence of V, O, C and Al in the entire region. However, more Al is visible in the discharged electrode than the charged one (Fig. S8e and Fig. S8j). Furthermore, ex-situ Raman measurements of bf-VEG/CC were also performed in pristine state, after 1st discharge and 1st charge. For pristine VEG, six characteristics bands located at 139 , 190 , 280 , 404 , 689 and 987 cm^{-1} were observed (Fig. 5c). After 1st discharge, the B3g band at 139 cm^{-1} is observed to shift to 141.2 cm^{-1} (Fig. 5d). Meanwhile, the band at 689 cm^{-1} and 987 cm^{-1} , ascribed to the stretching vibration of V-O mode also shifts to 692 cm^{-1} and 990 cm^{-1} (Fig. 5e and Fig. 5f). This shifting in Raman spectra could be related to the possible change in the bonding modes due to Al^{3+}

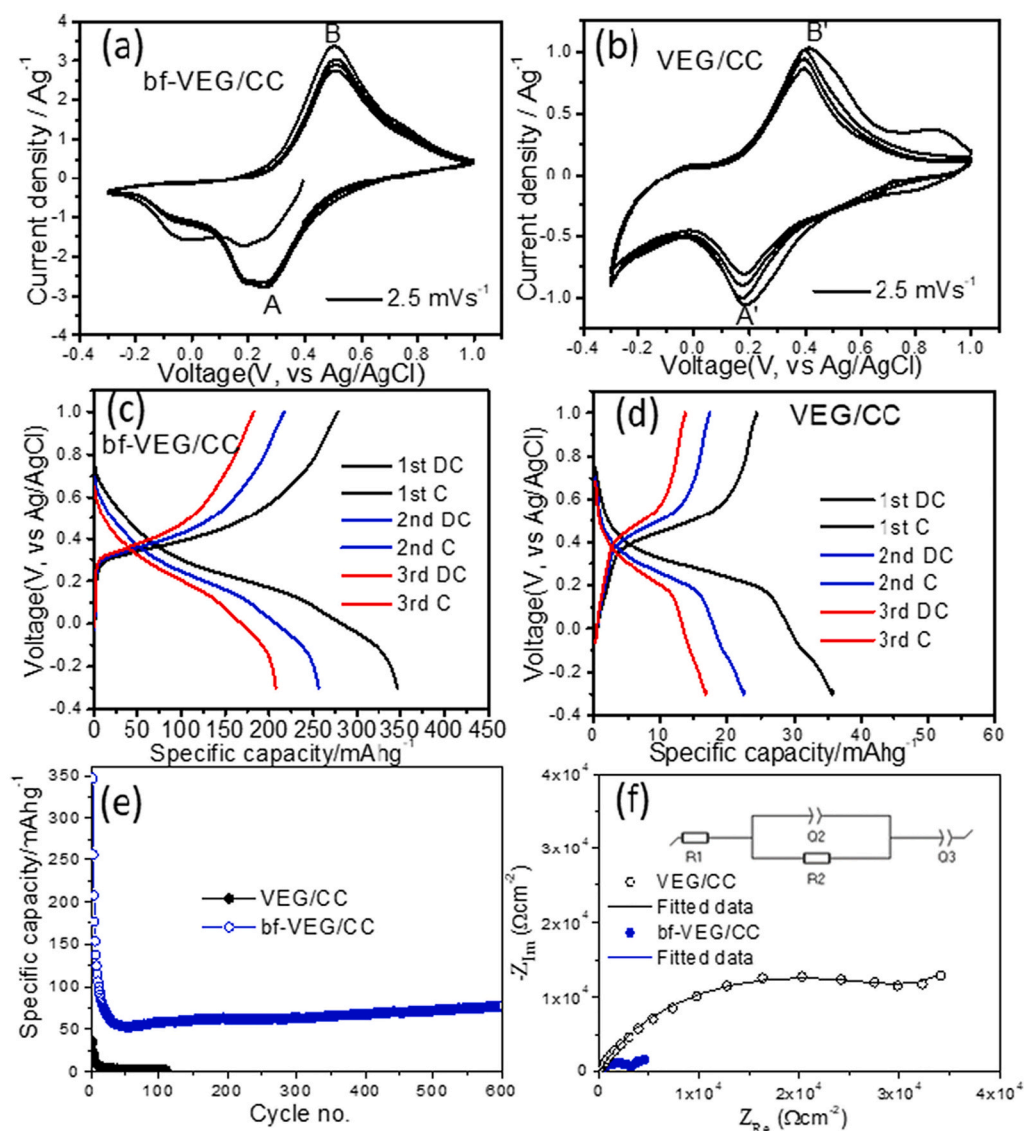


Fig. 2. CV curves of (a) bf-VEG/CC, (b) VEG/CC at a scan rate of 2.5 mVs^{-1} . Galvanostatic charge/discharge curves of (c) bf-VEG/CC, (d) VEG/CC, (e) Comparison of discharge capacities with cycle number at a current density of 2 Ag^{-1} , and (f) EIS spectra for VEG/CC and bf-VEG/CC respectively (Inset shows the equivalent circuit).

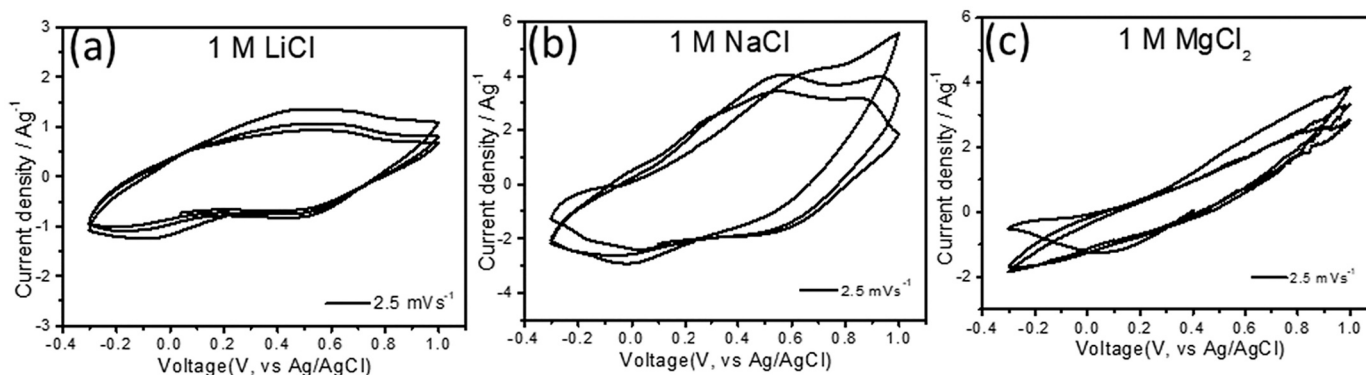


Fig. 3. CV curves of bf-VEG/CC in (a) 1 M LiCl, (b) 1 M NaCl, and (c) 1 M MgCl_2 aqueous electrolytes at a scan rate of 2.5 mVs^{-1} .

ion insertion [20]. Further, to understand the Al^{3+} ion storage behavior, CV of bf-VEG/CC were performed at different scan rates in 1 M AlCl_3 aqueous electrolyte (Fig. 6a). The diffusion controlled and capacitive

controlled contributions are estimated using the following standard equations: $I = av^b$ and $I = k_1v + k_2v^{1/2}$, where I is the redox peak currents, a and b are adjustable parameters, v is the scan rate, k_1 and k_2 are

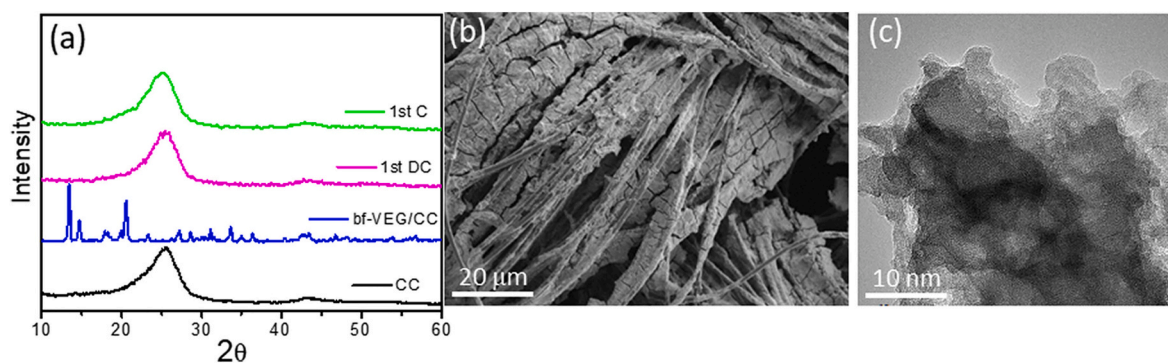


Fig. 4. (a) Ex-situ XRD patterns of bf-VEG/CC electrode before and after 1st discharge/charge. Ex-situ (b) SEM and (c) TEM images of bf-VEG/CC after 1st discharge.

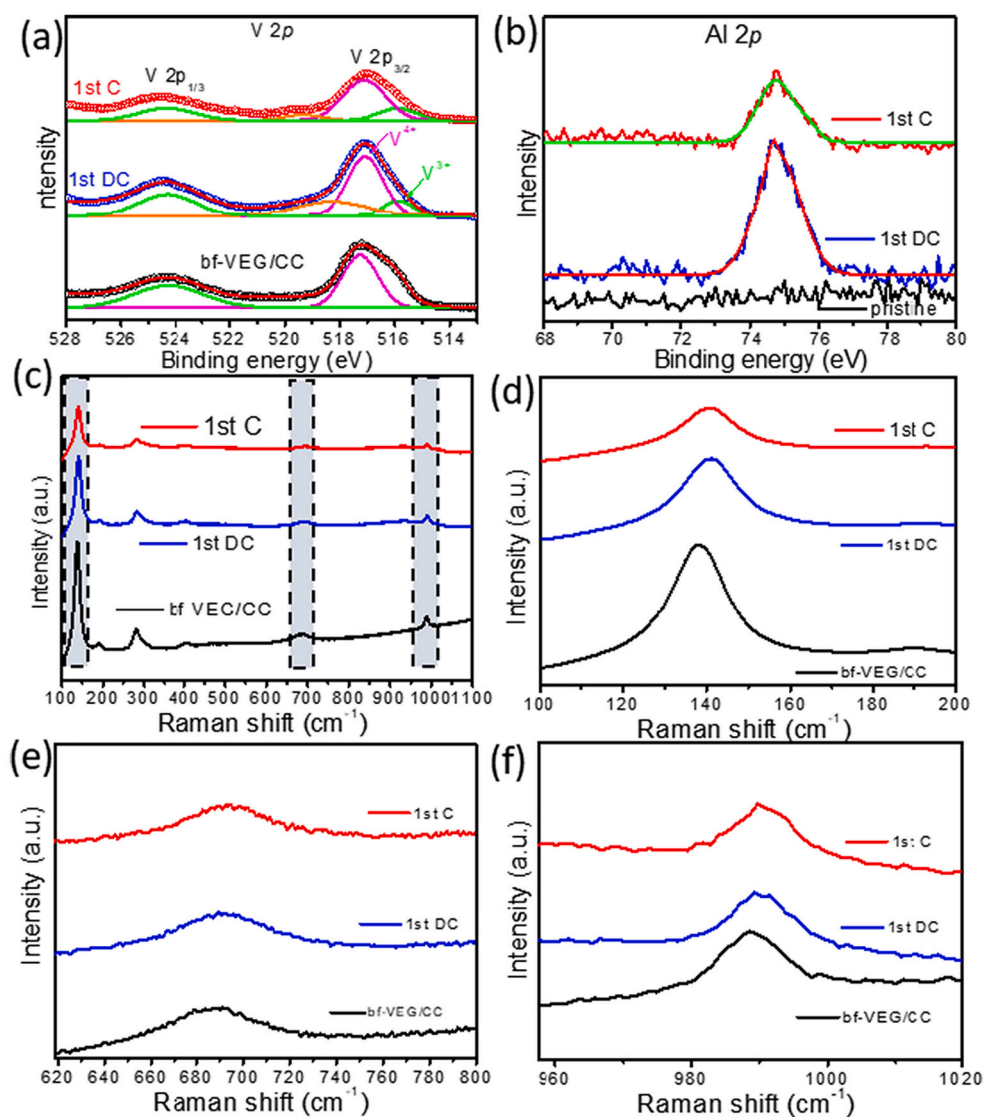


Fig. 5. (a) Ex-situ XPS spectra of V2p before discharge and after 1st discharge/1st charge state, (b) Ex-situ XPS spectra of Al 2p before discharge and after 1st discharge/1st charge state, and (c) ex-situ Raman spectra of bf-VEG/CC electrode before, after 1st discharge/1st charge state. (d-f) enlarged view of the dotted marked regions.

constants [37–38]. Here, k_1v and $k_2v^{1/2}$ respectively correspond to the contributions arising out of capacitive controlled and diffusion-controlled processes. It is found that the diffusion-controlled process is the most dominating process (Fig. 6b). For example, the olive color

region shown in Fig. 6c indicates the diffusion-controlled process at a scan rate of 2.5 mVs^{-1} which represents 83% of the total capacity. The ratio of these contributions at various scan rates are displayed in Fig. 6d. All these observations indicate possible Al^{3+} ion insertion and extraction

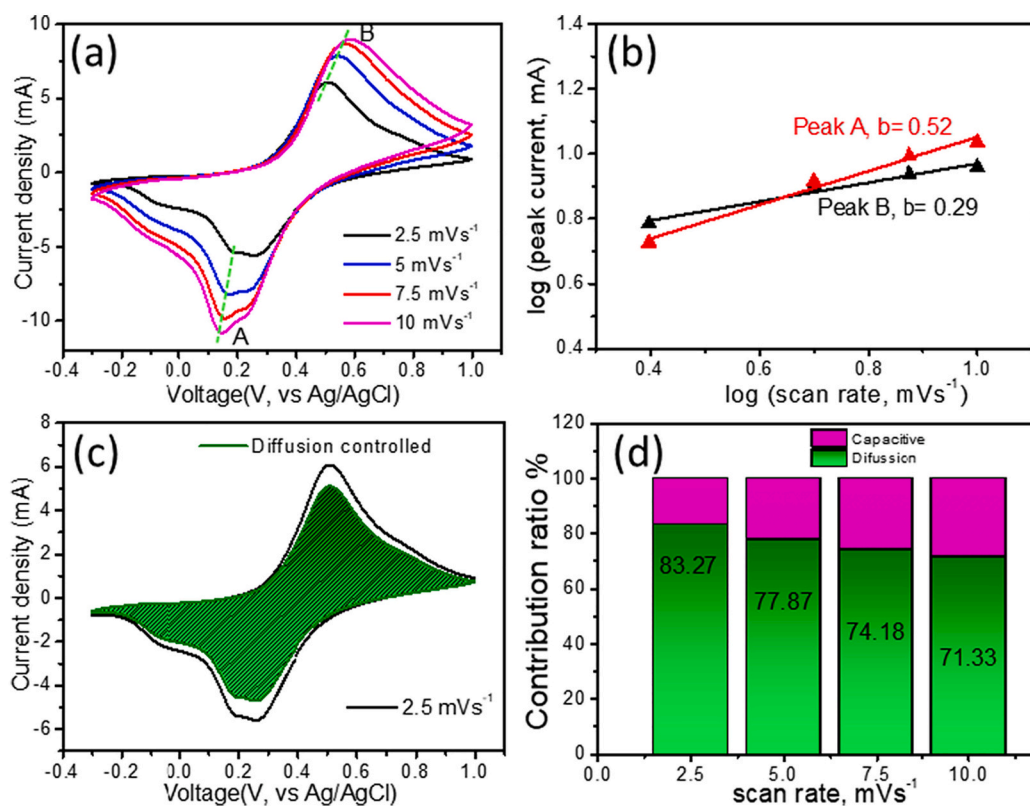


Fig. 6. CV curves of bf-VEG/CC electrode at different scan rates, (b) corresponding $\log(i)$ vs $\log(v)$ plots, (c) CV curve with the diffusion-controlled contribution at a scan rate of 2.5 mVs^{-1} , and (d) contribution ratios of diffusion and capacitive-controlled at various scan rates in 1 M AlCl_3 aqueous electrolyte.

in VEG. Based on these analysis, the following possible electrochemical reaction mechanism may occur during initial discharge process: $\text{VO}(\text{CH}_2\text{O})_2$ (crystalline) + $x\text{Al}^{3+}$ + $3x\text{e}^- \rightarrow (\text{Al}^{3+})_x[(\text{V}^{4+})_{(1-x)}(\text{V}^{3+})_x]\text{O}(\text{CH}_2\text{O})_2$ (amorphous). It is noted here that a deterministic value of x is not possible at this juncture since the final composition is unknown and the ex-situ XRD pattern also could not be analyzed due to lack of any diffraction peaks. However, if all the V^{4+} states transform to V^{3+} states due to Al^{3+} ion insertion, then $x = 1$ which results in a theoretical capacity of 623 mAhg^{-1} . It is noted here that there is a possible dissolution of the electrode material in the electrolyte. The change of color of the electrolyte from transparent (before cycling) to green and yellow after cycling hints at it (Fig. S9). Because of it, there may be a gradual decline of capacity during initial cycles. We harvested the electrolytes after 10th and 200th cycle and these were analyzed using UV-visible spectroscopy. An absorption band appears at 281 nm for 10th cycle electrolyte. On the other hand, another new absorption band appears at 294 nm for 200th cycle electrolyte. The exact physical origin of these peaks however could not be identified.

4. Conclusions

In summary, we designed a binder free VEG electrode and its Al^{3+} ion storage behavior in aqueous electrolyte is illustrated. The binder free electrode shows excellent long term cycling stability with specific capacity values of the order of 77 mAhg^{-1} over hundreds of cycles which was not possible in pristine form of VEG. It was also found that diffusion-controlled process dominated the Al^{3+} ion storage behavior.

CRediT authorship contribution statement

Sunny Nandi: Methodology, Data curation, Validation, Investigation, Writing – original draft, Writing – review & editing. **Yichen Yan:** Data curation, Formal analysis. **Xintong Yuan:** Data curation, Formal

analysis. **Chongzhen Wang:** Data curation, Formal analysis. **Ximin He:** Formal analysis, Writing – review & editing. **Yuzhang Li:** Conceptualization, Supervision, Writing – review & editing, Funding acquisition. **Shyamal K. Das:** Conceptualization, Supervision, Writing – review & editing, Funding acquisition.

Declaration of Competing Interest

The authors declare that they have no known competing financial interests or personal relationships that could have appeared to influence the work reported in this paper.

Data availability

Data will be made available on request.

Acknowledgement

SN acknowledge the financial support received from USIEF and IIE through Fulbright-Nehru Doctoral Research Fellowship 2021-2022 for enabling his stay at University of California, Los Angeles. The authors thank Jinhui Xu (Department of Chemical and Biomolecular Engineering, UCLA) for the XRD and TGA measurements. SKD acknowledges the financial support received from Science and Engineering Research Board, Department of Science and Technology, Government of India (Grant No.: CRG/2018/000263).

Appendix A. Supplementary data

Supplementary data to this article can be found online at <https://doi.org/10.1016/j.ssi.2022.116085>.

References

- [1] Y. Liang, H. Dong, D. Aurbach, Y. Yao, Current status and future directions of multivalent metal-ion batteries, *Nat. Energy* 5 (2020) 646–656, <https://doi.org/10.1038/s41560-020-0655-0>.
- [2] D. Monti, A. Ponrouch, R.B. Araujo, F. Barde, P. Johansson, M.R. Palacin, Multivalent batteries—prospects for high energy density: Ca batteries, *Front. Chem.* 7 (2019), <https://doi.org/10.3389/fchem.2019.00079>.
- [3] A. Ponrouch, J. Bitenc, R. Dominko, N. Lindahl, P. Johansson, M.R. Palacin, Multivalent rechargeable batteries, *Energy Storage Mater.* 20 (2019) 253–262, <https://doi.org/10.1016/j.ensm.2019.04.012>.
- [4] M.A. Schroeder, L. Ma, G. Pastel, K. Xu, The mystery and promise of multivalent metal-ion batteries, *Curr. Opin. Electrochem.* 29 (2021), 100819, <https://doi.org/10.1016/j.coelec.2021.100819>.
- [5] Y. Zhang, E.H. Ang, K.N. Dinh, K. Rui, H. Lin, J. Zhu, Q. Yan, Recent advances in vanadium-based cathode materials for rechargeable zinc ion batteries, *Mater. Chem. Front.* 5 (2021) 744–762, <https://doi.org/10.1039/D0QM00577K>.
- [6] Y. Kim, Y. Park, M. Kim, J. Lee, K.J. Kim, J.W. Choi, Corrosion as the origin of limited lifetime of vanadium oxide-based aqueous zinc ion batteries, *Nat. Commun.* 13 (2022) 2371, <https://doi.org/10.1038/s41467-022-29987-x>.
- [7] Q. Wang, J. Xu, W. Zhang, M. Mao, Z. Wei, L. Wang, C. Cui, Y. Zhu, J. Ma, Research progress on vanadium-based cathode materials for sodium ion batteries, *J. Mater. Chem. A* 6 (2018) 8815–8838, <https://doi.org/10.1039/C8TA01627E>.
- [8] H. Tang, Z. Peng, L. Wu, F. Xiong, C. Pei, Q. An, L. Mai, Vanadium-based cathode materials for rechargeable multivalent batteries: challenges and opportunities, *Electrochem. Energy Rev.* 1 (2018) 169–199, <https://doi.org/10.1007/s41918-018-0007-y>.
- [9] Y. Liu, X. Wu, Review of vanadium-based electrode materials for rechargeable aqueous zinc ion batteries, *J. Ener. Chem.* 56 (2021) 223–237, <https://doi.org/10.1016/j.jechem.2020.08.016>.
- [10] M.C. Lin, M. Gong, B. Lu, Y. Wu, D.Y. Wang, M. Guan, M. Angell, C. Chen, J. Yang, B.J. Hwang, H. Dai, An ultrafast rechargeable aluminium-ion battery, *Nature* 520 (2015) 324–328, <https://doi.org/10.1038/nature14340>.
- [11] H. Chen, H. Xu, S. Wang, T. Huang, J. Xi, S. Cai, F. Guo, Z. Xu, W. Gao, C. Gao, Ultrafast all-climate aluminum-graphene battery with quarter-million cycle life, *Sci. Adv.* 3 (2017) 7233–7241, <https://doi.org/10.1126/sciadv.aao7233>.
- [12] H. Sun, W. Wang, Z. Yu, Y. Yuan, S. Wang, S. Jiao, A new aluminium-ion battery with high voltage, high safety and low cost, *Chem. Commun.* 51 (2015) 11892–11895, <https://doi.org/10.1039/C5CC00542F>.
- [13] Mahdi Kazazi, Pedram Abdollahi, Mahdi Mirzaei-Moghadam, High surface area TiO₂ nanospheres as a high-rate anode material for aluminum-ion batteries, *Solid State Ionics* 300 (2017) 32–37.
- [14] H. Chen, F. Guo, Y. Liu, T. Huang, B. Zheng, N. Ananth, Z. Xu, W. Gao, C. Gao, Defect-free principle for advanced graphene cathode of aluminum-ion battery, *Adv. Mater.* 29 (2017) 1605958, <https://doi.org/10.1002/adma.201605958>.
- [15] S.K. Das, S. Mahapatra, H. Lahan, Aluminium-ion batteries: developments and challenges, *J. Mater. Chem. A* 5 (2017) 6347–6367, <https://doi.org/10.1039/C7TA00228A>.
- [16] S. He, J. Wang, X. Zhang, J.Z. Chen, Z.C. Wang, T.T. Yang, Z.W. Liu, Y. Liang, B. Y. Wang, S.Q. Liu, L.Q. Zhang, J.Y. Huang, J. Huang, L.A. O'Dell, H.J. Yu, A high-energy aqueous aluminum-manganese battery, *Adv. Funct. Mater.* 29 (2019), 905228, <https://doi.org/10.1002/adfm.201905228>.
- [17] C. Wu, S. Gu, Q. Zhang, Y. Bai, M. Li, Y. Yuan, H. Wang, X. Liu, Y. Yuan, N. Zhu, F. Wu, H. Li, L. Gu, J. Lu, Electrochemically activated spinel manganese oxide for rechargeable aqueous aluminum battery, *Nat. Commun.* 10 (2019) 1–10, <https://doi.org/10.1038/s41467-018-07980-7>.
- [18] N. Jayaprakash, S.K. Das, L.A. Archer, The rechargeable aluminum-ion battery, *Chem. Commun.* 47 (2011) 12610, <https://doi.org/10.1039/C1CC15779E>.
- [19] S. Liu, G.L. Pan, G.R. Li, X.P. Gao, Copper hexacyanoferrate nanoparticles as cathode material for aqueous Al-ion batteries, *J. Mater. Chem. A* 3 (2015) 959, <https://doi.org/10.1039/C4TA04644G>.
- [20] Q. Zhao, M.J. Zachman, W.I. Al Sadat, J. Zheng, L.F. Kourkoutis, L. Archer, Solid electrolyte interphases for high-energy aqueous aluminum electrochemical cells, *Sci. Adv.* 4 (2018) eaau8131, <https://doi.org/10.1126/sciadv.aau8131>.
- [21] H. Lahan, S.K. Das, An approach to improve the Al³⁺ ion intercalation in anatase TiO₂ nanoparticle for aqueous aluminum-ion battery, *Ionics* 24 (2018) 1855–1860, <https://doi.org/10.1007/s11581-018-2530-6>.
- [22] S. Nandi, S.K. Das, Realizing a low-cost and sustainable rechargeable aqueous aluminum-metal battery with exfoliated graphite cathode, *ACS Sustain. Chem. Eng.* 7 (2019) 19839–19847, <https://doi.org/10.1021/acssuschemeng.9b05185>.
- [23] S. Kumar, R. Satish, V. Verma, H. Ren, P. Kidkhunhod, W. Manalastas Jr., M., Srinivasan Investigating FeVO₄ as a cathode material for aqueous aluminum-ion battery, *J. Power Sources* 426 (2019) 151–161, <https://doi.org/10.1016/j.jpowsour.2019.03.119>.
- [24] Q. Zhao, L. Liu, J. Yin, J. Zheng, D. Zhang, J. Chen, Lynden archer, proton intercalation/de-intercalation dynamics in vanadium oxides for aqueous aluminum electrochemical cells, *Angew. Chem.* 59 (2020) 3048–3052, <https://doi.org/10.1002/anie.201912634>.
- [25] Y. Ru, S. Zheng, H. Xue, H. Pang, Potassium cobalt hexacyanoferrate nanocubic assemblies for high-performance aqueous aluminum ion batteries, *Chem. Eng. J.* 382 (2020), 122853, <https://doi.org/10.1016/j.cej.2019.122853>.
- [26] C. Weeks, Y. Song, M. Suzuki, N.A. Chernova, P.Y. Zavalij, M. Stanley Whittingham, The one dimensional chain structures of vanadyl glycolate and vanadyl acetate, *J. Mater. Chem.* 13 (2003) 1420–1423, <https://doi.org/10.1039/B208100H>.
- [27] X. Wang, X. Bi, S. Zheng, S. Wang, Y. Zhang, H. Du, J. Lu, High-rate performance and ultralong cycle life enabled by hybrid organic–inorganic vanadyl ethylene glycolate for lithium-ion batteries, *Adv. Energy Mater.* 8 (2018) 1801978, <https://doi.org/10.1002/aenm.201801978>.
- [28] Q. Li, Y. Zhu, Y. Yu, Y. Qian, Synthesis and transformation of vanadyl ethylene glycolate, and their applications in a lithium-ion battery, *Int. J. Electrochem. Sci.* 7 (2012) 5557–5564.
- [29] R. Nagaraj, S. Pakhira, K. Aruchamy, P. Yadav, D. Mondal, K. Dharmalingam, N. Sanna Kotrapannavar, D. Ghosh, Catalyzing the intercalation storage capacity of aqueous zinc-ion battery constructed with Zn(II) preinserted organo-vanadyl hybrid cathode, *ACS Appl. Energy Mater.* 3 (2020) 3425, <https://doi.org/10.1021/acsaem.9b02466>.
- [30] X. Li, J. Feng, N. Wen, S. Chen, Q. Kuang, Q. Fan, Y. Dong, Y. Zhao, High electrochemical performance of in-situ carbon-coated vanadyl ethylene glycolate as cathode for aqueous zinc-ion batteries, *Solid State Ionics* 364 (2021), 115632, <https://doi.org/10.1016/j.ssi.2021.115632>.
- [31] H. Lahan, S.K. Das, Al³⁺ ion intercalation in MoO₃ for aqueous aluminum-ion battery, *J. Power Sources* 413 (2019) 134–138.
- [32] L. Zhou, L. Yang, P. Yuan, J. Zou, Y. Wu, C. Yu, α-MoO₃ nanobelts: a high performance cathode material for lithium ion batteries, *J. Phys. Chem. C* 114 (2010) 21868–21872.
- [33] J. Joseph, A.P. O'Mullane, K. Ostrikov, Hexagonal molybdenum trioxide (h-MoO₃) as an electrode material for rechargeable aqueous aluminum-ion batteries, *ChemElectroChem* 6 (2019) 6002–6008.
- [34] H. Lahan, S.K. Das, Reversible Al³⁺ ion insertion into tungsten trioxide (WO₃) for aqueous aluminum-ion batteries, *Dalton Trans.* 48 (2019) 6337–6340.
- [35] D. Chao, W. Zhou, F. Xie, C. Ye, H. Li, M. Jaroniec, S.-Z. Qiao, Roadmap for advanced aqueous batteries: From design of materials to applications, *Sci. Adv.* 6 (2020) eba4098.
- [36] J.R. Gonzalez, F. Nacimiento, M. Cabello, R. Alcantara, P. Lavela, J.L. Tirado, Reversible intercalation of aluminium into vanadium pentoxide xerogel for aqueous rechargeable batteries, *RSC Adv.* 6 (2016) 62157–62164, <https://doi.org/10.1039/C6RA11030D>.
- [37] T. Brezesinski, J. Wang, S.H. Tolbert, B. Dunn, Ordered mesoporous α-MoO₃ with iso-oriented nanocrystalline walls for thin-film pseudocapacitors, *Nat. Mater.* 9 (2010) 146, <https://doi.org/10.1038/nmat2612>.
- [38] J. Wang, J. Polleux, J. Lim, B. Dunn, Pseudocapacitive contributions to electrochemical energy storage in TiO₂ (Anatase) nanoparticles, *J. Phys. Chem. C* 111 (2007) 14925–14931, <https://doi.org/10.1021/jp074464w>.